Waveguide Antenna Topologies for Distributed High-Frequency Near-Field Communication and Localization

Artem Voronov, Oleksiy Sydoruk, *Member, IEEE*, and Richard R. A. Syms, *Fellow, IEEE*

Abstract— High-frequency (HF) near-field communication (NFC) is an inherently short-range technology. However, the total capture volume can be increased with traveling-wave antennas. Here, we report on the analysis, design, and measurements of flexible waveguide antennas and discuss their performance for NFC and localization. The antennas comprise sections of coaxial transmission lines loaded periodically with field-generating inductive networks. Several topologies were compared to each other theoretically, and the best-performing candidate was selected to fabricate antennas between 5 and 48 m long, each containing 15 read nodes. Waveguiding properties of the antennas were measured and agreement with the theory was demonstrated. Afterward, each antenna was integrated with a custom NFC reader and shown to be capable of communication with and localization of commercial off-the-shelf transponders compliant with ISO/IEC 14443 Type A protocol. The transverse detection range was 10 cm with 1 W input RF power. Both 1-D and quasi-2-D configurations were tested. The proposed antennas are flexible, scalable, have low loss, and could be used for NFC, identification, and tracking of distributed and mobile tags.

Index Terms— High-frequency (HF), localization, near-field communication (NFC), radio-frequency identification (RFID), slow wave, transmission-line antenna.

I. INTRODUCTION

HIGH-FREQUENCY (HF) near-field communication (NFC) is a wireless technology that operates in the 13.56 MHz band and is used widely for asset management, access control, and secure payments [1]. A common embodiment contains an active reader that uses a magnetic near field to power and communicates with a passive transponder. Because near fields decay rapidly away from the reader and tag antennas, communication is inherently short-range. Range extension has been achieved with active transponders [2] or with higher-power readers [3], [4], but both methods are restricted by scaling laws.

The capture volume of loop antennas can be enhanced through geometry optimization [5], and further gains can be achieved by antenna arrays [6], albeit with additional hardware overhead. Arrangements allowing arbitrary tag orientations

[7], [8], and arrays with null zone compensation [9] have been demonstrated. Traveling-wave antennas have also been used for lateral increase of capture volume at no overhead cost to hardware complexity. The system presented in [10] was able to read off-the-shelf proximity tags compliant with ISO 14443 protocol along a 2.3-m-long antenna. The antenna was a section of magneto-inductive waveguide that comprised magnetically coupled resonant circuits [11], [12]. The read range perpendicular to the antenna was 50 cm with 10 W RF power. Further examples are magneto-inductive systems proposed for body-area networks [13], [14].

In addition to communicating with tags, large antenna systems may need to locate and track them. Potential applications include automated inventory management such as tracking of library books and warehouse contents, livestock monitoring, mobile robot pathfinding, and personnel or document tracking. The HF regime, however, offers limited possibilities for localization compared to ultra high frequency (UHF) radio-frequency identification (RFID) [15], [16], [17], which relies on radiative fields. Most research on HF positioning addresses the converse problem of localization of mobile objects within reference transponder grids. Such an object has often been a robot equipped with a single [18], [19] or multiple readers [20], [21], [22], [23], while the transponder distribution could be uniform or sparse [24]. Similar methods have been applied to identify the location and orientation of furniture [25]. When tag position was unknown, the localization methods have mostly been limited to scanning with moving antennas [26], [27], or multiplexed antenna arrays [28], [29], [30], [31]. One- [32] and 2-D [33] magnetic metamaterials have also been used to locate metallic resonators and wireless power devices.

Syms et al. [34] offered an alternative approach to localization, which relied on low group velocity in a magneto-inductive wave antenna. A signal generated by a transponder propagates in two opposite directions along the antenna. Receivers placed at both antenna ends detect the signals with a measurable delay, and the transponder position along the antenna can be estimated from the time-of-arrival (TOA) difference. This system can be upscaled by adding more elements to the waveguide antenna, without increasing the hardware overhead.

Unfortunately, magneto-inductive waveguides suffer from relatively high propagation loss and from layout restrictions imposed by the need to achieve high coupling strengths between resonant elements [35]. Both aspects limit potential

TABLE I

NFC Tag Localization Techniques

Ref.	Located Object	Antenna Type	Reader number	Range	System complexity scales with	Power
[26]	Books	1 mobile antenna	1, with probabilistic localization	N/A	Shelf layout	High
[27]	Books	2 mobile antennas	1, with probabilistic localization	N/A	Room layout	High
[28]	Encapsulated tag	2 x 2 elmt. flexible array	1, with multiplexer	11.1 cm	Elmt. number	2W
[29]	Glass tags	21 elmt. array	1, with cascaded multiplexers	4 cm	Elmt. number	1-5W
[30]	Glass tags	6 x 5 elmt. array	2, with 16 channels each	10 cm	Elmt. number	0.5-8W
[31]	NFC Speedtap™ tags	5 x 5 elmt. active array	1, but elmts. have separate oscillators	3 cm	Elmt. number	280 mW
[34]	ISO 14443 tags	1-D magneto-inductive traveling-wave antenna	1, with TOA localization	6 cm	Fixed	1W
This work	ISO 14443 tags	1-D or quasi-2-D LTL traveling-wave antenna	1, with TOA localization	10 cm	Fixed	1W

deployment, for example, when transponders are distributed sparsely or over a long distance. However, other waveguides are also capable of supporting slow waves. Well-known examples are left- and right-handed waveguides that contain periodic lumped-element sections [36], [37] or electrically small resonators [38]. Therefore, waveguides that both support slow waves at HF and comprise inductors that couple to NFC transponders have potential as antennas. The aim of this article is to explore candidate waveguide antennas and demonstrate their use in NFC communication and localization. Table I compares existing solutions with the one proposed in this work.

Section II analyzes transmission lines made of coaxial cables loaded periodically with two-port inductive networks, discusses design criteria and tradeoffs, and selects a suitable antenna topology. Section III discusses measurements of antenna parameters and compares them to theoretical models. Sections IV and V present experimental results for NFC communication and localization using 1-D and quasi-2-D antennas. Section VI discusses system scalability. Section VII draws a conclusion.

II. Design of LTLs

This section provides a theoretical analysis of waveguide antennas formed by sections of transmission lines (such as coaxial cables) loaded periodically with lumped-element networks. The networks must contain inductors that generate a magnetic near field and can couple to an NFC device placed in their vicinity. We will refer to these networks as sensors and to the entire waveguides as loaded transmission lines (LTLs). In this article, we derive characteristic equations of LTLs and discuss how their properties can be optimized for HF near-field transponder localization.

A. Two-Port Cascades

First, we briefly state known properties of a periodic cascade of two-port networks shown in Fig. 1(a) [39]. The networks can be modeled by a 2×2 transmission matrix $\boldsymbol{P} = [A, B; C, D]$. A current I_n at an angular frequency ω flows into the nth network that has a voltage V_n across its left-side terminals. The voltages and currents on either side of the two-port are related by
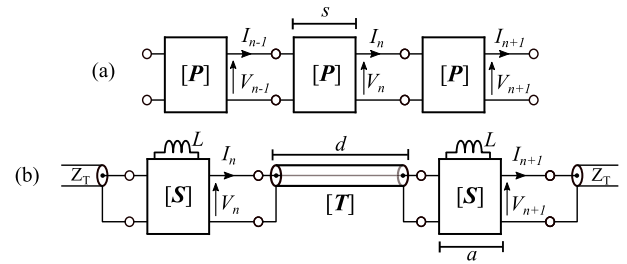

Fig. 1. Schematic of (a) classical periodic cascade of two-port networks, each having a transfer matrix $\boldsymbol{P}$. (b) LTL formed by a periodic cascade of coaxial cable sections and generic two-port networks having transmission matrices $\boldsymbol{T}$ and $\boldsymbol{S}$, respectively.

$$\begin{bmatrix} V_n \\ I_n \end{bmatrix} = \begin{bmatrix} A & B \\ C & D \end{bmatrix} \begin{bmatrix} V_{n+1} \\ I_{n+1} \end{bmatrix}. \quad (1)$$

This periodic structure can support waves, with voltages and currents satisfying relationships $V_{n+1} = V_n e^{-jks}$ and $I_{n+1} = I_n e^{-jks}$, where k is the propagation constant, and s is the length of a network. Nontrivial solutions of (1) exist when

$$e^{j2ks} - (A + D)e^{jks} + AD - BC = 0. \quad (2)$$

Equation (2) is the dispersion relation for the two-port cascade. If $\boldsymbol{P}$ is reciprocal, then det $\boldsymbol{P} = 1$, and (2) can be simplified as

$$\cos(ks) = \frac{A + D}{2}. \quad (3)$$

The propagation constant is generally complex and frequency dependent. However, if $\boldsymbol{P}$ is lossless, A and D are real, while B and C are imaginary. Propagation may only occur in passbands for which $|\cos(ks)| < 1$, so that $\Im(k) = 0$. Propagation is forbidden in stopbands, where k is purely imaginary. If a network contains lossy components, attenuated out-of-band propagation is allowed.

The voltages and currents at any plane of the cascade are related by a characteristic impedance defined as

$$Z_{\mathrm{P}} = \frac{V_n}{I_n} = \frac{B}{e^{jks} - A}. \quad (4)$$

The values of Z_P are different for forward- and backward-wave propagation. In lossless symmetrical networks, Z_P is real in the passband and imaginary in the stopbands.

B. Loaded Transmission Lines

We now consider the LTL shown schematically in Fig. 1(b). A unit cell is formed by a section of a coaxial cable of length d, followed by a reciprocal two-port network $S = [A_S, B_S; C_S, D_S]$ of length a. Together they correspond to the earlier P.

The cable can be described as a lossy transmission line with an inductance per unit length L_T and capacitance per unit length C_T. The cable transmission matrix T is of the form

$$T = \begin{bmatrix} \cos(\gamma d) & j Z_T \sin(\gamma d) \\ (j/Z_T) \sin(\gamma d) & \cos(\gamma d) \end{bmatrix} \quad (5)$$

where Z_T is the cable characteristic impedance. The cable propagation constant is complex, $\gamma = \beta - j\alpha$, with $\beta \approx \omega\sqrt{L_T C_T}$.

The unit cell of the LTL has a transmission matrix $P = TS$ and a length $s = d + a$. Using (3) and (4), we obtain an LTL dispersion relation in the form

$$\cos ks = \frac{1}{2}\left\{(A_S + D_S)\cos(\gamma d) + j\left(\frac{B_S}{Z_T} + Z_T C_S\right)\sin(\gamma d)\right\}. \quad (6)$$

The characteristic impedance of the LTL can be rewritten as

$$Z_0 = \frac{B_S \cos(\gamma d) + j Z_T D_S \sin(\gamma d)}{e^{jks} - [A_S \cos(\gamma d) + j Z_T C_S \sin(\gamma d)]}. \quad (7)$$

C. Sensor Network Topologies

Equations (6) and (7) model generic LTL waveguides, and candidate networks S should now be identified that are suitable for HF NFC, identification, and localization. Requirements are set by communication protocols, and we will use the common ISO 14443 standards for proximity cards [40]. The reader carrier frequency is $f_c = 13.56$ MHz. In Type A systems, signals are transmitted from the reader to a transponder by amplitude modulation of the carrier using on-off-keying at a bit rate of $f_c/128$ bit/s. The transponder responds by load-modulation using sub-carriers separated from f_c by $f_s = f_c/16$ at the same bit rate. The minimum bandwidth is $BW = 2f_s + f_c/32 = 5f_c/32 = 2.12$ MHz, where the first term is the subcarrier separation, and the second is the approximate bandwidth required for Manchester encoded data transmission. If a waveguide antenna is used, its dispersion should be minimized to prevent signal distortion. On the other hand, the localization method of [34] relies on being able to detect the difference in arrival times of transponder signals. To maximize this difference, the group velocity of the waveguide should be minimized.

Fig. 2 shows schematically idealized characteristics of a waveguide antenna optimized for both communication and transponder localization. The dispersion curve [Fig. 2(a)] is linear (to eliminate dispersion), and propagation occurs in a passband (to minimize the group velocity). The passband is equal to 2.12 MHz. The group velocity $v_g = (\partial\omega)/(\partial k)$ can
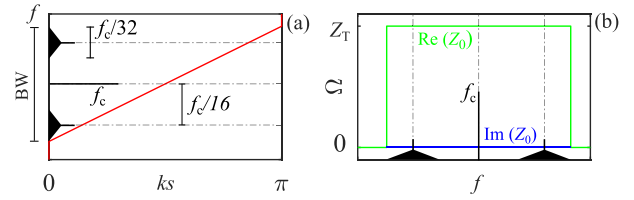

Fig. 2. (a) Dispersion curve and (b) characteristic impedance (green and blue) of an idealized LTL antenna for transponder tracking and communication. The passband covers the communication bandwidth of ISO/IEC 14443 Type A protocol. The group velocity is constant and minimized. The characteristic impedance is real and constant across the passband.
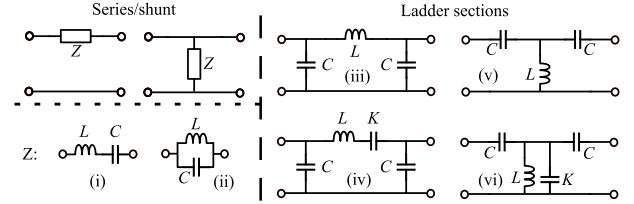

Fig. 3. Sensor network candidates that include series/shunt impedances (i) and (ii), pi-sections (iii) and (iv), and t-sections (v) and (vi).

be calculated from the idealized dispersion characteristic as $[\pi/(s \cdot 2\pi \cdot BW)]^{-1} = 5/16 f_c \cdot s = 4.24 \times 10^6 \cdot s$ m/s. The slow-wave factor (SWF $= c/v_g$, where c is the free-space light velocity) is $16c/(5f_c s) = 70.8/s$, where the numerator is in meters. The characteristic impedance over the passband must be real and equal to Z_T, independently of the cable length used [Fig. 2(b)]. Fig. 2 shows characteristics of a right-handed waveguide, but the arguments apply also to a left-handed one.

Such characteristics are unattainable in practice but can serve to assess practical sensor implementations. Possibilities are shown in Fig. 3, in the order of increasing complexity. The simplest LTL topologies comprise a shunt or a series impedance Z. The impedance itself can be either (i) a series or (ii) a parallel LC resonator. Topologies (iii) and (v) are, respectively, the standard lumped-element pi- and t-sections of right- and left-handed transmission lines. Topologies (iv) and (vi) are constructed from (iii) and (v) by adding another capacitor K. Analytical calculations presented in this section will assume lossless wave propagation; effects of loss will be considered in Section III.

For LTLs made of coaxial cables loaded with impedances Z in a series or a shunt configuration, we have $A_S = D_S = 1$. Cable sections of non-zero length are required for wave propagation. Equation (6) can be simplified as

$$\cos ks = \cos \beta d + \frac{1}{2} jr \sin \beta d \quad (8)$$

where $r = Z/Z_T$ for the series and $r = Z_T/Z$ for the shunt configurations.

Fig. 4(a) shows the real part of the propagation constant and Fig. 4(b) shows the slow-wave factor for (i) series and (ii) parallel LC resonators connected in series and shunt configurations, respectively, with $C_T = 92$ pF/m, $L_T = 230$ nH/m, and $Z_T = 50$ Ω. In both cases, $L = 2$ μH, and the value of C is chosen to place the resonant frequency at 13.56 MHz. The cable length d is 4 m. Both cases exhibit a
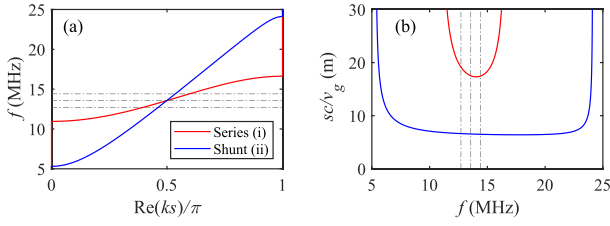
Fig. 4.   (a) Dispersion relation and (b) slow-wave factor for LTL waveguide loaded with impedances (i) and (ii) in series and shunt configurations, respectively, for $L = 2$ μH, $C = 68.9$ pF, and $d = 4$ m. Dashed lines show the frequency locations of HF carrier and tag response sidebands.

Fig. 5.   (a) Dispersion curves and (b) slow-wave factors for LTL antennas with $d = 2$ m loaded with sections (iii)–(vi). For (iii) $L = 0.59$ μH, $C = 250$ pF; (iv) $L = 2$ μH, $C = 115$ pF, $K = 89.7$ pF; (v) $L = 0.59$ μH, $C = 200$ pF; and (vi) $L = 0.37$ μH, $C = 190$ pF, $K = 143$ pF. Topology (iv) offers the best match to the ideal requirements of Fig. 2(a).

bandpass response, and the bandwidth depends on the cable length and the value of L.

For both configurations, increasing the cable length narrows the passband and shifts it down in frequency. The effect is more pronounced at higher frequencies. For the series configuration, a larger value of L reduces the upper cut-off frequency but has little effect on the lower cut-off. Conversely, a larger value of L increases the upper cut-off frequency for the shunt configuration. The characteristic impedance $Z_0 = Z_T$ at f_c for both configurations. Series loading with (i) favors high values of L, while shunt loading with (ii) requires impractically small L to achieve a similar SWF. Series (ii) and shunt (i) loads are not considered as they cannot have $Z_0 = Z_T$ within their passband at any frequency.

The LTL becomes a ladder network with cable interconnects when the sensors are formed by a pi- or a t-section shown in Fig. 3(iii)–(vi). Denoting k_0 as the propagation constant for a cascade of sensors with no cables, we can express the LTL propagation constant, k, in terms of k_0, and the cable propagation constant, β. For a symmetric pi- or t-section, $\cos(k_0 a) = A_S$ according to (3), and the characteristic impedance is $Z_S = B_S/[j \sin(k_0 a)]$ according to (4), while $C_S = (A_S D_S - 1)/B_S$ owing to reciprocity. Equation (6) can then be rewritten as

$$\cos(ks) = \cos(k_0 a) \cos(\beta d) - \frac{1}{2} \sin(k_0 a) \left(\frac{Z_S}{Z_T} + \frac{Z_T}{Z_S} \right) \sin(\beta d). \tag{9}$$

Equation (9) shows that $k \approx k_0$ for short cables, but long cables affect the value of k owing to the second term on the right-hand side of (9). The impedances Z_S and Z_T can always be made equal at a single frequency, for example, f_c. Fig. 5 shows the dispersion curves and the slow-wave factor for cable sections of length $d = 2$ m. The pi-section (iii) has a low-pass response while the t-section (v) has a high-pass one. The presence of cable sections lowers the cut-off frequencies for both topologies. It also converts the high-pass response of a CL section (v) into a bandpass one. Topology (iii) offers good linearity if the cut-off frequency is sufficiently higher than the upper sideband frequency, but higher slow-wave factors may be achievable with (v) owing to its bandpass characteristic. The maximum inductor values of both (iii) and (v) are restricted by the simultaneous need to keep the sideband frequencies within the LTL passband and to match the impedances at f_c.

All sensor topologies considered approximate to a different degree the ideal characteristics shown in Fig. 2. Series loading
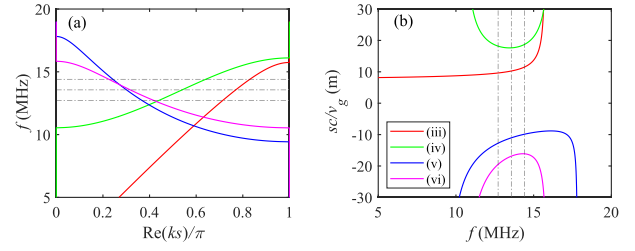
with (i) offers a bandpass response with good linearity and high SWF. However, this topology leaves little freedom for dispersion engineering since the value of C is restricted by matching requirements. The value of d can be restricted by the geometry of a specific application, and the value of L may be constrained by the need to generate magnetic fields. Topologies (iv) and (vi) have an additional degree of freedom offered by the capacitance K. Both topologies (iv) and (vi) have a bandpass response; topology (vi) supports backward waves and topology (iv) forward waves. Topology (iv), however, favors higher values of L.

D. Resonant LC Pi-Section

Of all the topologies considered, the pi-section (iv) in Fig. 3 is the closest match for the communication and localization requirements of Fig. 2, and it offers the largest design freedom. Fig. 6 shows calculated frequency variations of (a) dispersion, (b) slow-wave factor, and (c) and (d) real and imaginary parts of the characteristic impedance for several values of cable length d. The LTL is perfectly matched to $Z_S = Z_T = 50$ Ω at f_c independently of d. The matching condition is given by

$$K = \frac{1 + \omega_c^2 C^2 Z_T^2}{\omega_c^2 (C Z_T^2 (\omega_c^2 LC - 2) + L)} \tag{10}$$

where $\omega_c = 2\pi f_c$. Capacitance K introduces an additional degree of freedom, allowing L and C to be set independently to tailor dispersion while retaining matching at f_c if (10) is satisfied. The cable length affects the cut-off frequencies and the group velocity. Because longer cables reduce the original passband and shift it to lower frequencies, practical cable lengths are limited by the need to accommodate the NFC frequencies inside the passband.

If $Z_T = Z_S$ at f_c, then $ks = \beta d + k_0 a$ according to (9), and expressions for the group velocity and SWF at f_c can be derived as

$$v_g = \frac{s}{d\sqrt{L_T C_T} + \frac{2\omega LC}{\sin(k_0 a)}} \tag{11}$$

$$\text{SWF} = \frac{c}{s} \left(d\sqrt{L_T C_T} + \frac{2\omega LC}{\sin(k_0 a)} \right). \tag{12}$$

Equations (11) and (12) suggest that in a matched antenna the total slow-wave effect is the sum of individual contributions from the cables and the sensors.
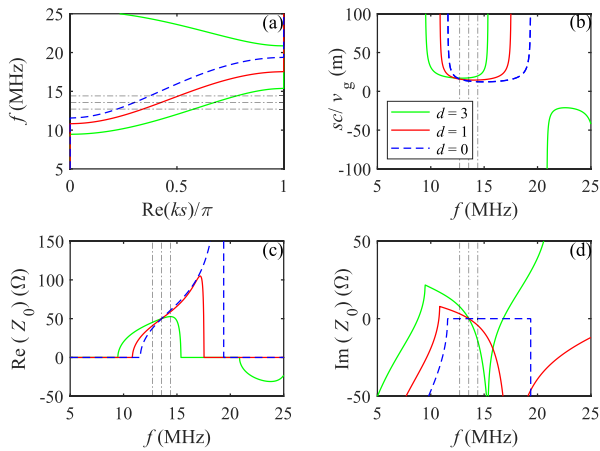
Fig. 6. Parameters of the LTL antenna with resonant LC pi-section for cable lengths of $d = 0$, 1, and 3 m: (a) dispersion relation; (b) slow-wave factor; (c) real part of the characteristic impedance; and (d) imaginary part of the characteristic impedance. Usable cable lengths are limited by the need to accommodate the NFC frequencies inside the passband. Sensors have $L = 1.75$ µH, $C = 120$ pF, and $K = 108$ pF.

III. EXPERIMENTAL CHARACTERIZATION OF LTLs

This section describes the fabrication and experimental characterization of LTL waveguides with resonant LC pi-section sensors. Three waveguides were made by cascading 15 identical sensors with coaxial cables of three different lengths, 0.3, 1.22 (4 ft), and 3 m. Fig. 7 shows a photograph of a section of an assembled LTL, together with the equipment (a PC, electronics for signal transmission, an oscilloscope for signal reception and filters for signal separation) used in communication and localization experiments described in Sections IV and V.

Table II shows the component values, the equivalent sensor circuit, and the cable parameters. The inductance L was formed by a three-turn square spiral with rounded corners, made from 1/8" soft copper pipe that was bent to shape and held in place using 3-D-printed acrylonitrile butadiene styrene (ABS) mounts. The spiral had a width of W = 130 mm and a winding separation of 5 mm. The quality factor was measured as $\approx$250 using a vector network analyzer (Keysight E5061B) connected to two small inductive probes coupled to the assembled inductors. In these experiments, the inductors were loaded with capacitors, so that the resonant frequency was equal to f_c.

A printed circuit board of a width of 30 mm was then inserted laterally into the plastic mount and served to interconnect the three inductive windings and the capacitors forming C and K, as well as to provide SMA connections to coaxial cables. Capacitance K was implemented using a symmetrical pair of $2K$ capacitors and a small varicap for precision impedance matching at f_c. The parasitic capacitance C_p was found as 4.1 pF across all inductors. The component values were chosen to optimize the LTL characteristics for a cable length of $d = 1.22$ m. To demonstrate that the waveguide topology offered significant design freedom, shorter and longer cables were also used, without changing the sensors. All three sets of cables had characteristic impedances of 50 Ω, with RG-174 Telegartner used for the short (0.3 m) cables, and
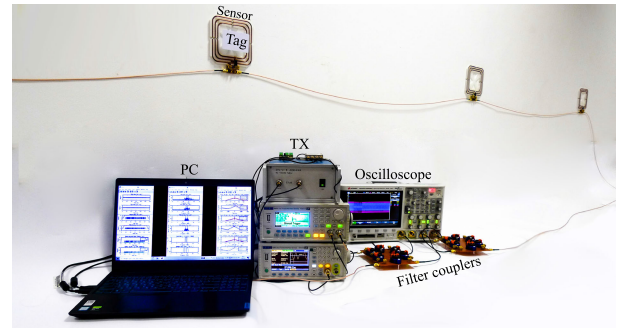

Fig. 7. Photograph of the complete NFC system including an LTL antenna and a custom reader.

TABLE II
SENSOR AND CABLE PARAMETERS

Sensors		Cables		
L (µH)	1.73	Type	RG-174	RG-316
C (pF)	120	d (m)	0.30	1.22; 3.00
K (pF)	103	Z_T (Ω)	50	
C_P (pF)	4.12	C_T (pF/m)	105	95
Q	250	v_g/c	66%	69.5%
		10 MHz atten. (dB/100m)	9.5	8.86
		Dielectric	PE	Teflon®

RG-316 Cinch Connectors used for the medium-long (1.22 m) and long (3 m) cables.

The sensors were individually tuned to minimize reflectivity at f_c as measured by the network analyzer. Subsequently, the cable interconnects were introduced, and the scattering parameters of the entire LTL were measured. With 15 sensors, the total waveguide lengths were 5.25, 20.0, and 48.5 m for the small, medium, and long cables, respectively. The number of elements was chosen to be large enough so that effects of dispersion and loss could be observed. Having an odd number of elements provided a convenient midpoint for the localization experiments described in Sections IV and V.

Fig. 8(a) compares the theoretical propagation constant calculated using (6) (dashed lines) with measured data (crosses). Fig. 8(b) shows the measured group delay. Fig. 8(c)–(h) show the measured (solid lines) and theoretical (dashed lines) S-parameters. The results for the short cables are shown in blue, for the medium-long cables in red, and for the long cables in green. The theoretical curves were obtained by first computing the equivalent transmission matrix for each of the three antenna configurations as $P^N T$ with $N = 15$, followed by an S-parameter conversion. Excellent agreement is seen across the figures. The slight deviations in S_{21} below the lower cut-off for short and medium cables can be attributed to cable effects and have been eliminated for long cables by placing ferrimagnetic rings to impede current flow on the outside surfaces of the cable shields. As expected, longer cables both reduce and shift the passband lower in frequency. Good matching is retained at f_c regardless of the cable length. The measured group delay is flat between the two sidebands for the medium-long cables but is sloping for the short and long cables. Despite performance degradation for the short and long cables, all three cable lengths are suitable for NFC
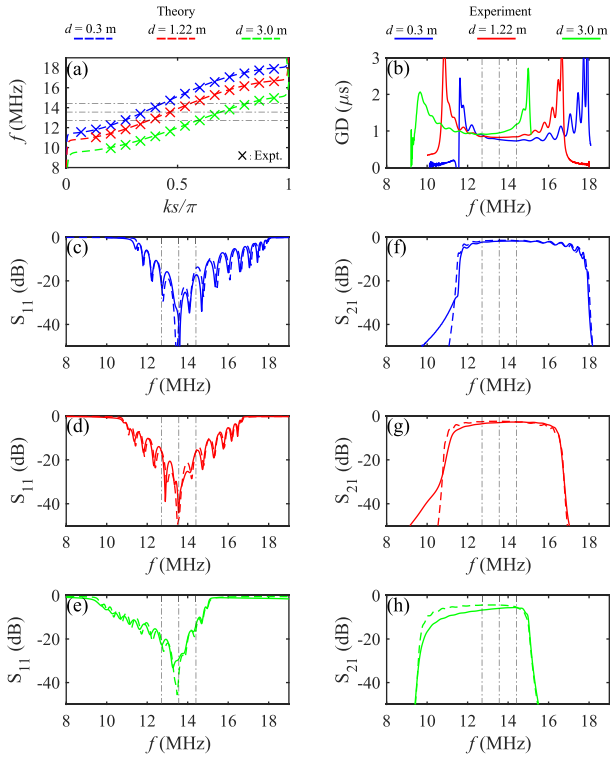
Fig. 8. Characteristics of LTLs with cable sections of $d = 0.3$ m (blue), $d = 1.22$ m (red), $d = 3$ m (green): (a) measured (crosses) and theoretical (dashed lines) LTL propagation constant, (b) measured group delay, and (c)–(h) measured (solid lines) and simulated (dashed lines) S-parameters. Agreement between theory and experiment is excellent. The best-performing waveguide has $d = 1.22$ m, but the other two waveguides are also suitable for NFC.

applications. The loss at f_c is 0.35, 0.15, and 0.12 dB/m for the short, medium-long, and long cables, respectively. The higher value for the short cables is caused by a higher relative contribution of the sensors. The same behavior can be observed for the group delay, which is dominated by the slow wave effect of the sensors. While the group delay can be improved by reducing the passband, doing so would restrict the range of possible cable lengths.

IV. NEAR-FIELD LOCALIZATION WITH 1-D ANTENNAS

This section discusses experiments on the localization of NFC transponders by TOA difference. The localization method was introduced in [34]. Fig. 9 shows a functional block diagram of the system; the previous Fig. 7 shows a photograph. An ISO/IEC 14443 Type A compliant tag was placed next to one of the sensors along the antenna. A custom reader, capable of transmitting and receiving a subset of signals according to ISO/IEC 14443 Type A protocol, injected an HF carrier at one end of the antenna using a frequency-selective filter-coupler [41]. The carrier propagated along the antenna, and the current circulating in the spiral inductors generated magnetic near fields. The other end of the antenna was connected to an identical filter-coupler.

The reader then sent a unique identifier (UID) query (in modified Miller code, using amplitude shift key carrier modulation). The tag transmitted its UID by sub-carrier load modulation (in Manchester code). The tag response propagated
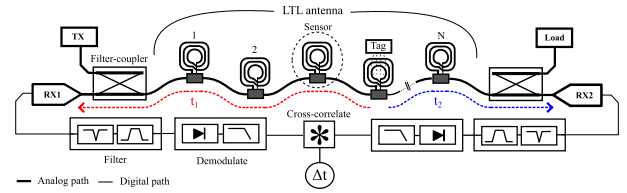

Fig. 9. Block diagram for NFC system capable of tag localization along LTL antenna.

toward both ends of the antenna, where the filter-couplers extracted the carrier signal, and the UID response was acquired by two receivers, each applying residual carrier and out-of-band noise suppression filters followed by rectification and low-pass filtering for UID demodulation. After a pair-wise cross correlation on the baseband UID responses, the TOA difference $\Delta t = t_2 - t_1$ was calculated from the cross-correlation peaks. The theoretical value of the LTL group velocity v_g at sideband frequencies was then used to convert Δt into a physical tag position estimate $P_{est} = P_m - \Delta t \cdot v_g$, where $P_m = (1 + N)/2$ is the midpoint sensor position, and $N = 15$ is the total number of elements in the LTL.

The reader transmitter comprised a pair of phase-locked function generators and an RF switch (Mini-Circuits ZASWA-2-50DRA+). One generator (TTi TG4042) was used for the HF carrier, and the other (TTi TG5012A) was used for modulation sequences. A 1 W amplifier (Mini-Circuits ZHL-2-8) amplified signals before injection into the LTL antenna. The tag responses were acquired with a digital oscilloscope (Keysight InfiniiVision DSOX3024T, sampling rate 1.25 GSa/s), while noise suppression, demodulation, and cross correlation were done in MATLAB using a PC. The matched filter couplers were custom-made using magneto-inductive waveguide sections and had a complementary bandpass–bandstop response at the carrier frequency [41]. Tags were placed above the midpoint of a spiral inductor, and tag-to-antenna separation was fixed by dielectric spacers.

Fig. 10 shows an error in tag position estimation ($e = P_{est} - P$) for each node index P over a range of sensor–tag separation distances using 1 W HF carrier power. Fig. 10(a)–(c) are for the antennas made with short, medium-long, and long cables, respectively. Each data point (circle) corresponds to a single TOA measurement using a Mifare 1 K Classic card-type tag with UID 0xF38AE495 and dimensions 85×55 mm. For all waveguides, the tag position was determined correctly ($|e| < 0.5$) over a sensor–tag separation from 1 to 10 cm, so that the correct position index could be obtained by rounding P_{est} to the nearest integer. The variation in e is the smallest for the medium-long cables and largest for the long cables. The results conform to expectations based on the measured antenna dispersion characteristics and scattering parameters (Fig. 8) and based on the fact that the sensors were optimized for the medium-long cables.

The tag UID could be decoded correctly for separations below 11 cm. Each waveguide demonstrates a consistent error profile, which marginally deteriorates for larger separations. These results suggest that the error variability is inherent to the antennas and not caused by noise. Tags with different
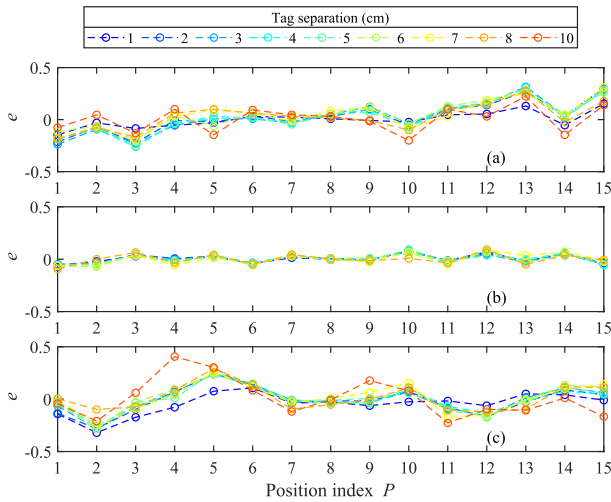
Fig. 10. Experimental variation of localization error e with tag position index P over a range of sensor–tag separation distances. (a) $d = 0.3$, (b) $d = 1.22$, and (c) $d = 3$ m.
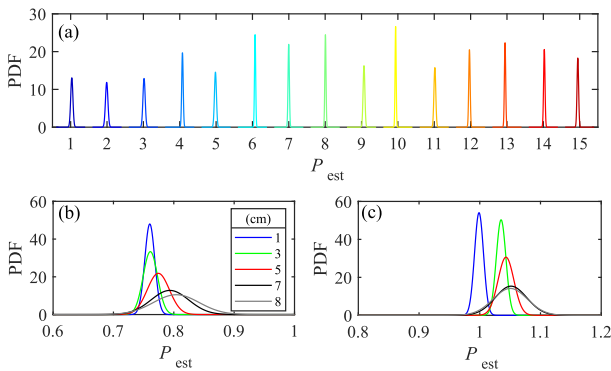

Fig. 11. pdfs fit to experimental position data using a sample size of 100 for each distribution. (a) Tag at 0 cm separation for all 15 sensors with $d = 1.22$ m. (b) Tag at varying separation distances at position 1 with $d = 0.3$ m. (c) Tag at varying separation distances at position 1 with $d = 3.0$ m. The tag could be located correctly for all measurements.

UIDs showed comparable error variation. Smaller tags (such as 1-in diameter fobs) had expectedly shorter detection ranges, but produced the same error variability profiles. If multiple transponders were present along the antenna, ISO/IEC 14443 Type A anticollision protocols could be used to sequentially request transponder UIDs for positioning.

Fig. 11(a) shows probability density functions (pdfs) fit using normal distributions to 100 samples of P_{est} at each node with the tag placed directly on top of a sensor, using 1 W carrier power, and the antenna with the medium-long cables. The position estimates are both highly consistent and resistant to background noise, as is evident from the extremely narrow distributions. There was negligible change in mean values and a marginal increase in variances for larger tag separations. Fig. 11(b) and (c) show pdfs fit using 100 position estimates at the first node for the antennas with the short and long cables, respectively, over a range of sensor–tag separations. For both antennas, the uncertainty in P_{est} increases with separation, owing to reduced signal-to-noise ratio (SNR). A slight upward shift in the pdf mean values can be seen, consistent with Fig. 10. The shift can be attributed to a slight variation in
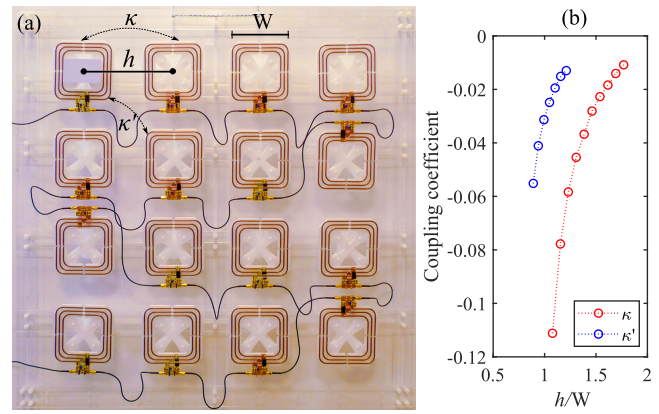

Fig. 12. (a) Photograph of a quasi 2-D LTL antenna. (b) Measured magnetic coupling coefficient between nearest neighbors, κ for adjacent elements (red) separated by h/W, and κ' for diagonally adjacent elements (blue).

waveguide group delay caused by weaker antenna loading by a more distant tag. The effects of changing the tag-to-antenna range were more pronounced for suboptimal cable length. Nevertheless, the variance was still low at all nodes which guaranteed accurate positioning.

V. NEAR-FIELD LOCALIZATION WITH QUASI-2-D ANTENNAS

This section extends the discussion of tag localization to quasi-2-D antennas. These were formed by rearranging an LTL into a 2-D grid while maintaining sequential cable interconnects. Fig. 12(a) shows an LTL forming a planar 4×4 grid, in which each row was connected to the next, and the inductor centers are separated by distance h. Coupling coefficients $\kappa = 2M/L$ and $\kappa' = 2M'/L$ were defined, where M was the mutual inductance between a pair of nearest neighbors, and M' was the mutual inductance between a pair of diagonal neighbors. Fig. 12(b) shows how measured values of the coupling coefficients decay with increasing normalized distances h/W. For $h/W > 1.456$, $|\kappa| < 0.03$, and κ' was negligibly small, so that the quasi-2-D antenna can be expected to perform like a 1-D one.

Fig. 13 shows scattering parameters, group delay, and per-element phase advance of the 2-D grid with $d = 1.22$ m. As the element separation h increased from 19 to 26 cm, the value of S_{11} at the carrier frequency was reduced by 10 dB, while the value of S_{21} increased by 0.8 dB. Similarly, the variation of the group delay between the sideband frequencies reduced as h increased. Further reductions in h resulted in significantly poorer matching and group velocity dispersion, while further increases saw scattering parameters converge to those of the 1-D antennas shown in Fig. 8. Presumably, the effects at small h are caused by non-nearest neighbor coupling [42].

Fig. 14 shows error variation in estimated tag positions for the 2-D grid over the same range of h. Fig. 14(a) shows e for a card-type tag with UID 0xF38AE495 at 1 cm range, while Fig. 14(b) is for a fob-type tag with UID 0x010D354A placed directly on top of the inductors. Both tags could be correctly located at all positions for $h \geq 19$ cm. The fob tag
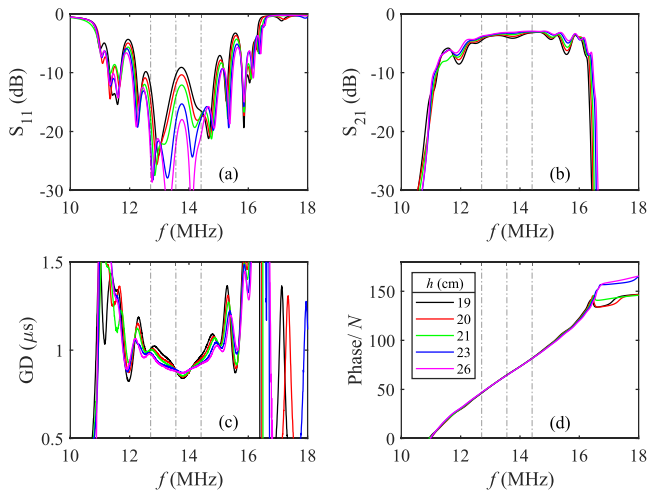
Fig. 13. Measured scattering parameters of quasi-2-D grid for a range of neighbor separation distances h. (a) S_{11} parameters. (b) S_{21} parameters. (c) Group delay. (d) Phase shift per element in degrees.
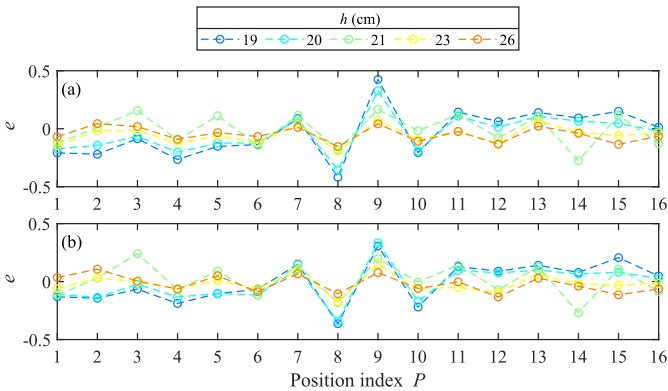

Fig. 14. Experimental variation of location error e with tag position index P over a range of neighbor separation distances h for (a) card-type and (b) fob-type tag.

on average saw a slight reduction in location error compared to the card tag, caused by a weaker antenna loading by a smaller fob. Stronger loading may introduce local variations of group velocity in the antenna around the contact point owing to asymmetry, thus resulting in higher errors. The shape of the error variation profiles was again nearly identical for the two tags, suggesting the errors were determined by local group velocity variations within the antenna. Tags placed between inductors could not be accurately located but could still be read.

VI. SYSTEM SCALABILITY

The lengths of our waveguide antennas were limited by the constraints of a laboratory experiment. This section discusses achievable antenna sizes. A limit will be imposed by waveguide attenuation and dispersion, which corrupt signals generated by tags. The effects were simulated in MAT-LAB[1] using a model adopted from [34]. A tag injected an amplitude-modulated signal $s(t) = \sin(2\pi f_c t)[1 + m(t)]$ into the nth element of the antenna, where $m(t)$ is the
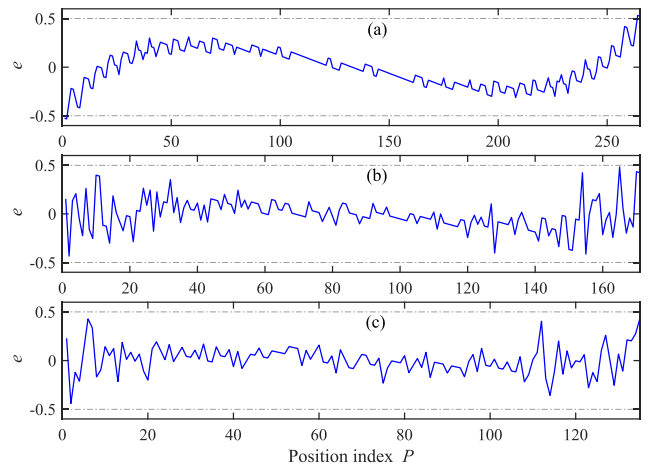
[1]Registered trademark.

Fig. 15. Simulated tag location detection error: (a) noiseless antenna with $N = 265$, (b) SNR = 30 dB with $N = 171$, and (c) SNR = 25 dB with $N = 135$.

subcarrier-modulated tag UID encoded in Manchester code according to the ISO/IEC14443 Type A protocol. The message signal was generated as $m(t) = a_m u(t) \sin(2\pi f_c t/16)$, where $u(t)$ was the binary UID signal, and a_m the amplitude. The tag signal $s(t)$ was then propagated to both ends of the antenna, taking antenna loss and dispersion into account, and uncorrelated white noise $n(t)$ was added to the signals prior to filter-couplers (see Fig. 9). A sampling rate of $8f_c$ was used, and the tag UID was 0x010D354A. The SNR was defined as

$$\text{SNR} = 10 \log \left(\frac{\sum_{i=1}^{J} \left| \left[m(t) \sin(2\pi f_c t) \right] * f(t) \right|^2}{\sum_{i=1}^{J} |n(t) * f(t)|^2} \right) \quad (13)$$

where $f(t)$ is the impulse response of the filter-couplers, J is the number of samples, and the asterisk represents linear convolution. The SNR, so defined, describes the ratio of the power of the tag signal at the entry to the waveguide to the noise power within the passbands of the filters. The signal power at each end is generally different, and such a definition avoids the need for two SNR values. For antennas with large N, high SNR may be needed to offset propagation losses. The maximum antenna length was determined by requiring that the tag localization error does not exceed half an element.

Fig. 15 shows localization error against tag position for $d = 1.22$ m. Fig. 15(a) assumes no noise, and the error profile is anti-symmetric around the midpoint sensor, where the error is zero. The exact shape arises owing to the combined effect of dispersion and smoothing during tag response down-conversion. The error was maximum for tags at antenna extremes because only one of the outputs was affected by dispersion. Fig. 15(b) and (c) shows localization error in the presence of receiver noise, with SNR of 30 and 25 dB, respectively. The maximum achievable line length became shorter as SNR was reduced, with the error once again being highest at antenna ends. The effect became more pronounced for antennas with higher loss. The maximum number of sensors for each configuration was 265, 171, and 135, respectively. Correlated noise, such as radio frequency interference picked up by sensors, is not included in the simulation, but its effects have been discussed previously [34].

TABLE III
MAXIMUM NUMBER OF ANTENNA ELEMENTS FOR DIFFERENT SNRs

	$d = 0.3$ m	$d = 1.22$ m	$d = 3.0$ m
Noiseless & Lossless	235	281	139
Noiseless & Lossy	195	265	121
SNR = 25 dB	171	135	79
SNR = 20 dB	141	107	63
SNR = 15 dB	93	73	45
SNR = 10 dB	67	51	31
SNR = 5 dB	19	17	13

Table III gives an overview of the other cable lengths used and different values of SNR. As can be expected, the optimized geometry with 1.22-m cables performs the best, and antennas exceeding 100 elements are feasible for the values of SNR above 20 dB. At low SNRs, tags could still be located but their UIDs could no longer be read correctly. This is explained by higher processing gain in UID cross correlation, as opposed to the bit-wise correlation required for UID decoding. Achieving high values of SNR as well as being able to power tags via long lossy antennas would require increased carrier powers.

VII. CONCLUSION

Our experiments and theoretical analysis suggest that the waveguide topologies considered in this article can be employed for practical NFC systems that require communication with and localization of distributed transponders, using a single set of electronics. The maximum antenna length realized experimentally was 48 m, and theoretical estimates show that antennas of several 100 s of meters are feasible with favorable SNR. The maximum read node separation demonstrated here was 3 m. This separation can be increased to system dimensions by interspersing functional and nonfunctional nodes, in the process allowing the functional nodes to be irregularly spaced. A simple learning algorithm may then be used to identify the functional nodes. In contrast to multiplexed antenna systems, increasing the number of read nodes carries no hardware overhead. The antennas are flexible and can be arranged in different shapes, as demonstrated by a quasi-2-D grid arrangement. Furthermore, localization to the nearest node was found to be accurate irrespective of the range or tag type used, provided the field was strong enough to power the tag.

The localization method used is based on comparing the TOA of tag signals reaching both ends of an antenna. The antennas were consequently optimized for low group velocity, with the associated drawback of increased propagation loss. Scenarios that do not require tags to be localized impose less stringent requirements on waveguiding properties of antennas, which could as a result be made longer and rely on simpler topologies. On the other hand, the need to extract signals from both antenna ends limits deployment options by requiring lengthy return cables and two receivers. Single-ended localization systems may offer additional flexibility with sensor layout, reduce system complexity, and remove the need for a return cable. The feasibility of such systems should be assessed in future work.

REFERENCES

[1] K. Finkenzeller, *RFID Handbook*, 3rd ed. Chichester, U.K.: Wiley, 2010.

[2] K. Finkenzeller, F. Pfeiffer, and E. Biebl, "Range extension of an ISO/IEC 14443 type a RFID system with actively emulating load modulation," in *Proc. 7th Eur. Workshop Smart Objects, Syst., Technol. Appl.*, Dresden, Germany, May 2011, pp. 1–10.

[3] I. Kirschenbaum and A. Wool, "How to build a low-cost, extended-range RFID skimmer," in *Proc. 15th USENIX Secur. Symp.*, Vancouver, BC, Canada, Jul. 2006, pp. 43–57.

[4] J. Zirbesegger, M. Gebhart, E. Merlin, and E. Leitgeb, "Extending the analogue performance of integrated 13.56 MHz proximity reader chips," *Elektrotechnik Informationstechnik*, vol. 124, no. 11, pp. 369–375, Nov. 2007.

[5] W. Aerts, E. De Mulder, B. Preneel, G. A. E. Vandenbosch, and I. Verbauwhede, "Dependence of RFID reader antenna design on read out distance," *IEEE Trans. Antennas Propag.*, vol. 56, no. 12, pp. 3829–3837, Dec. 2008.

[6] A. Boryssenko and E. Boryssenko, "Antenna array design for HF RFID smart cabinet," in *Proc. IEEE Int. Conf. Microw., Commun., Antennas Electron. Syst. (COMCAS)*, Nov. 2011, pp. 1–3.

[7] M. Benamara et al., "A twisted loop antenna to enhance HF RFID detection for different tag positioning," in *Proc. 10th Eur. Conf. Antennas Propag. (EuCAP)*, Apr. 2016, pp. 1–5.

[8] M. Benamara, M. Grzeskowiak, M. Salhi, G. Lissorgues, A. Diet, and Y. Le Bihan, "3D HF RFID reader antenna for tag detection in different angular orientations," in *Proc. Loughborough Antennas Propag. Conf. (LAPC)*, Nov. 2016, pp. 1–4.

[9] H. Hirayama, Y. Satake, N. Kikuma, and K. Sakakibara, "Improvement of null zone avoidance capability for HF-band RFID using diversity combining of loop antennas," in *Proc. 3rd Eur. Conf. Antennas Propag.*, Mar. 2009, pp. 1594–1597.

[10] R. R. A. Syms, O. Sydoruk, and M. C. K. Wiltshire, "Magneto-inductive HF RFID system," *IEEE J. Radio Freq. Identificat.*, vol. 5, no. 2, pp. 148–153, Jun. 2021.

[11] E. Shamonina, V. A. Kalinin, K. H. Ringhofer, and L. Solymar, "Magnetoinductive waves in one, two, and three dimensions," *J. Appl. Phys.*, vol. 92, no. 10, pp. 6252–6261, Oct. 2002.

[12] E. Shamonina, V. A. Kalinin, K. H. Ringhofer, and L. Solymar, "Magneto-inductive waveguide," *Electron. Lett.*, vol. 38, no. 8, pp. 371–373, Apr. 2002.

[13] V. Mishra and A. Kiourti, "Wearable magnetoinductive waveguide for low-loss wireless body area networks," *IEEE Trans. Antennas Propag.*, vol. 69, no. 5, pp. 2864–2876, May 2021.

[14] A. Hajiaghajani, A. H. A. Zargari, M. Dautta, A. Jimenez, F. Kurdahi, and P. Tseng, "Textile-integrated metamaterials for near-field multibody area networks," *Nature Electron.*, vol. 4, no. 11, pp. 808–817, Nov. 2021.

[15] L. M. Ni, D. Zhang, and M. R. Souryal, "RFID-based localization and tracking technologies," *IEEE Wireless Commun.*, vol. 18, no. 2, pp. 45–51, Apr. 2011.

[16] J. Zhou and J. Shi, "RFID localization algorithms and applications—A review," *J. Intell. Manuf.*, vol. 20, no. 6, pp. 695–707, Aug. 2008.

[17] C. Li, L. Mo, and D. Zhang, "Review on UHF RFID localization methods," *IEEE J. Radio Freq. Identificat.*, vol. 3, no. 4, pp. 205–215, Dec. 2019.

[18] K. Yamano, K. Tanaka, M. Hirayama, E. Kondo, Y. Kimuro, and M. Matsumoto, "Self-localization of mobile robots with RFID system by using support vector machine," in *Proc. IEEE/RSJ Int. Conf. Intell. Robots Syst. (IROS)*, vol. 4, Sep. 2004, pp. 3756–3761.

[19] S. Park and S. Hashimoto, "Indoor localization for autonomous mobile robot based on passive RFID," in *Proc. IEEE Int. Conf. Robot. Biomimetics*, Feb. 2009, pp. 1856–1861.

[20] K. Kodaka, H. Niwa, Y. Sakamoto, M. Otake, Y. Kanemori, and S. Sugano, "Pose estimation of a mobile robot on a lattice of RFID tags," in *Proc. IEEE/RSJ Int. Conf. Intell. Robots Syst.*, Sep. 2008, pp. 1385–1390.

[21] S. Han, H. Lim, and J. Lee, "An efficient localization scheme for a differential-driving mobile robot based on RFID system," *IEEE Trans. Ind. Electron.*, vol. 54, no. 6, pp. 3362–3369, Dec. 2007.

[22] M. Y. Ahmad and A. S. Mohan, "Novel bridge-loop reader for positioning with HF RFID under sparse tag grid," *IEEE Trans. Ind. Electron.*, vol. 61, no. 1, pp. 555–566, Jan. 2014.

[23] J. Mi and Y. Takahashi, "Low cost design of HF-band RFID system for mobile robot self-localization based on multiple readers and tags," in *Proc. IEEE Int. Conf. Robot. Biomimetics (ROBIO)*, Dec. 2015, pp. 194–199.

[24] P. Yang, W. Wu, M. Moniri, and C. C. Chibelushi, "Efficient object localization using sparsely distributed passive RFID tags," *IEEE Trans. Ind. Electron.*, vol. 60, no. 12, pp. 5914–5924, Dec. 2013.

[25] A. A. N. Shirehjini and S. Shirmohammadi, "Improving accuracy and robustness in HF-RFID-based indoor positioning with Kalman filtering and Tukey smoothing," *IEEE Trans. Instrum. Meas.*, vol. 69, no. 11, pp. 9190–9202, Nov. 2020.

[26] I. Ehrenberg, C. Floerkemeier, and S. Sarma, "Inventory management with an RFID-equipped mobile robot," in *Proc. IEEE Int. Conf. Autom. Sci. Eng.*, Sep. 2007, pp. 1020–1026.

[27] L. Xu, J. Liu, X. Wang, H. Gong, Y. Wang, and L. Chen, "HF RFID-based book localization via mobile scanning," in *Proc. 17th Annu. IEEE Int. Conf. Sens., Commun., Netw. (SECON)*, Jun. 2020, pp. 1–9.

[28] X. Li, J. Sidén, H. Andersson, and T. Schön, "A paper-based screen printed HF RFID reader antenna system," *IEEE J. Radio Freq. Identificat.*, vol. 2, no. 3, pp. 118–126, Sep. 2018.

[29] A. C. Alba et al., "Use of passive radio frequency identification technologies to monitor nest usage in the northern carmine bee-eater (*Merops n. Nubicus*)," *Zoo Biol.*, vol. 38, no. 6, pp. 498–507, Dec. 2019.

[30] M. van der Sluis, Y. de Haas, B. de Klerk, T. B. Rodenburg, and E. D. Ellen, "Assessing the activity of individual group-housed broilers throughout life using a passive radio frequency identification system—A validation study," *Sensors*, vol. 20, no. 13, p. 3612, Jun. 2020.

[31] Y. Mehlman, P. Kumar, M. Ozatay, S. Wagner, J. C. Sturm, and N. Verma, "Large-area electronics HF RFID reader array for object-detecting smart surfaces," *IEEE Solid-State Circuits Lett.*, vol. 1, no. 8, pp. 182–185, Aug. 2018.

[32] J. Yan, C. J. Stevens, and E. Shamonina, "A metamaterial position sensor based on magnetoinductive waves," *IEEE Open J. Antennas Propag.*, vol. 2, pp. 259–268, 2021.

[33] I. Khromova, C. Stevens, and E. Chatziantoniou, "Load localisation," Patent WO 2020/128 520 A1, Jun. 25, 2020.

[34] R. R. A. Syms, A. Voronov, and O. Sydoruk, "HF RFID tag location using magneto-inductive waves," *IEEE J. Radio Freq. Identificat.*, vol. 6, pp. 347–354, 2022.

[35] R. R. A. Syms, I. R. Young, and L. Solymar, "Low-loss magneto-inductive waveguides," *J. Phys. D, Appl. Phys.*, vol. 39, no. 18, p. 3945, 2006.

[36] T. Itoh and C. Caloz, *Electromagnetic Metamaterials: Transmission Line Theory and Microwave Applications*. Hoboken, NJ, USA: Wiley, 2005.

[37] G. V. Eleftheriades and K. G. Balmain, *Negative-Refraction Metamaterials: Fundamental Principles and Applications*. Hoboken, NJ, USA: Wiley, 2005.

[38] L. Solymar and E. Shamonina, *Waves in Metamaterials*. Oxford, U.K.: Oxford Univ. Press, 2009.

[39] L. Brillouin, *Wave Propagation in Periodic Structures: Electric Filters and Crystal Lattices*, vol. 2. New York, NY, USA: Dover, 1953.

[40] *Cards and Security Devices for Personal Identification—Contactless Proximity Objects*, Standard ISO/IEC 14443, 2018.

[41] A. Voronov, R. R. A. Syms, and O. Sydoruk, "High-performance magnetoinductive directional filters," *Electronics*, vol. 11, no. 6, p. 845, Mar. 2022.

[42] R. R. A. Syms, O. Sydoruk, E. Shamonina, and L. Solymar, "Higher order interactions in magneto-inductive waveguides," *Metamaterials*, vol. 1, no. 1, pp. 44–51, Mar. 2007.

Artem Voronov received the M.Eng. degree in electrical and electronic engineering from Imperial College London, London, U.K., in 2018, where he is currently pursuing the Ph.D. degree with the Department of Electrical and Electronic Engineering.

His current research interests include RFID and electromagnetic sensing.
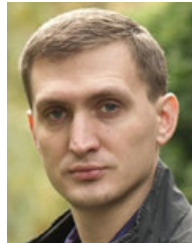
Oleksiy Sydoruk (Member, IEEE) received the B.Sc. degree in applied physics and the M.Sc. degree in radiophysics and electronics from the Taras Shevchenko National University of Kyiv, Kyiv, Ukraine, in 2002 and 2004, respectively, and the Ph.D. degree in physics from the University of Osnabrück, Osnabrück, Germany, in 2007.

He has been a Senior Lecturer with the Department of Electrical and Electronic Engineering, Imperial College London, London, U.K., since 2018. He has published in the areas of metamaterials, plasmonics, nanomaterials, and biomedical, polarization, and imaging optics. His current research interests include electromagnetic sensing.

Dr. Sydoruk is currently a Chartered Engineer.

Richard R. A. Syms (Fellow, IEEE) received the B.A. and D.Phil. degrees in engineering science from Oxford University, Oxford, U.K., in 1979 and 1982, respectively.

He has been a Professor of microsystems technology with the Department of Electrical and Electronics Engineering, Imperial College London, London, U.K., since 1996. He has developed many sensors based on integrated devices and co-founded the Imperial spin-out company Microsaic Systems, U.K., (which manufactures desktop mass spectrometers) in 2001. He has published widely on micro- and nano-engineering, bioengineering, holography, guided wave optics, metamaterials, and electromagnetic theory.

Prof. Syms is a fellow of the Royal Academy of Engineering, the Institute of Physics, and the Institute of Electrical and Electronic Engineers.